Climatic patterns over the European Alps during the LGM derived from inversion of the paleo-ice extent

Vjeran Višnjević[a,*], Frédéric Herman[a], Günther Prasicek[b]

[a]*Institute of Earth Surface Dynamics, University of Lausanne*
[b]*Interdisciplinary Center for Mountain Research, University of Lausanne*

Abstract

Quaternary climate has been dominated by alternating glacial and interglacial periods. While the timing and extent of past ice caps are well documented, local variations in temperature and precipitation as a response to cyclic glaciations are not resolved. Resolving these issues is necessary for understanding regional and global climate circulation. In particular, the impact of the cold high-pressure zone above the Fennoscandian ice cap on the position of the jet stream in Europe, and a possible change in the direction and the source of moisture flow are still discussed. Here we reconstruct climate conditions that led to the observed ice extent in the European Alps during the last glacial maximum (LGM). Using a new inverse method to reconstruct the spatially variable position of the equilibrium line altitude (ELA), we investigate whether southern shifts in the position of the Westerlies may have influenced the growth and retreat of the ice cap. We report inversion results that enable us to estimate the role of climate, inversion method parameters, ice dynamics, flexure and topography in modulating the inferred equilibrium line altitude. Our main finding is the presence of a dominating W-E gradient in the position of the ELA during the LGM that does not require a shift of the westerlies during the LGM.

Keywords: Alps, ice caps, paleoclimate, glacier mass balance, equilibrium line altitude, ice extent

---

*Corresponding author: vjeran.visnjevic@unil.ch

1. Introduction

The last glacial maximum (LGM), spanning from 26.5 ka to 20 ka (Clark et al., 2009), represents the last large dominating cold period with its legacy still imprinted on the present-day topography (e.g., Clark et al., 2009). The advent of numerical models (climate (Strandberg et al., 2011), ocean (Mikolajewicz, 2011), glacial (Seguinot et al., 2018), vegetation (Janská et al., 2017)), the development of new methods and an increase in available proxy data (pollen, SST, speleothems) open opportunities to improve our understanding of the climate conditions during the LGM and the interplay between glacial and climate processes that led to these conditions.

A significant body of work on LGM climate conditions in Europe provides estimates on precipitation and temperature patterns. Yet, uncertainties remain, highlighted by the discrepancies that exist between proxy data and models (Jost et al., 2005; Ramstein et al., 2007). Pollen-based reconstructions (Peyron et al., 1998) suggest a mean annual temperature depression, compared to today, of 12 ± 3°C, a mean coldest month depression of 30 ± 10°C, and a decrease in mean annual precipitation of 800 ± 100 mm (60 ± 20% lower than today). In contrast, modeling studies suggest warmer conditions compared to the observations inferred from pollen (Jost et al., 2005; Kageyama et al., 2006; Ramstein et al., 2007; Wu et al., 2007; Strandberg et al., 2011), especially in winter where the discrepancy is up to 10°C for western Europe (Ramstein et al., 2007). However, both pollen analysis (Peyron et al., 1998) and glacier modeling (Heyman et al., 2013; Seguinot et al.,

2018) indicate a 33% decrease in precipitation and a west-east temperature gradient during the LGM.

Another unresolved question is the position and intensity of storm tracks during the LGM over Europe (Florineth and Schlüchter, 2000; Kageyama et al., 2006; Kuhlemann et al., 2008; Hofer et al., 2012; Luetscher et al., 2015). Three end-member scenarios have been proposed. First, the LGM was dominated by westerly winds like today, but drier (Peyron et al., 1998; Kageyama et al., 2006). Second, there was an overall southward deflection of the jet stream (Florineth and Schlüchter, 2000). Such a shift may be explained by the breaking of the Rossby waves west of the Alps and the influence of the Fennoscandian ice sheet (Florineth and Schlüchter, 2000; Luetscher et al., 2015) and would have resulted in the meridional flow of moisture over the Alps from the Mediterranean (Florineth and Schlüchter, 2000; Kuhlemann et al., 2008; Hofer et al., 2012; Luetscher et al., 2015; Monegato et al., 2017). Third, Kuhlemann et al. (2008) proposed that the precipitation pattern was dominated by increased cyclogenesis, both in frequency and intensity, in the western Mediterranean. However, the influence of seasonality and the potential alternation between the zonal (during warm seasons) and meridional (during cold seasons) circulation remains unresolved (Kuhlemann et al., 2008). In any case, the characteristics of the Alpine climate during the LGM should be reflected in the position of the equilibrium line altitude (ELA) across the Alps and thus in LGM ice thickness and extent.

Ice extent and ice thickness over the Alps during the LGM are constrained by field observations from trimlines, moraines and erratic boulders, as well as from dating of glacial deposits (Bini et al., 2009; Ehlers et al., 2011). Such data serve as both input and validation basis for glacial modeling of the region (Jouvet et al., 2008; Becker et al., 2016; Cohen et al., 2017; Seguinot et al., 2018). Recently, several in-depth modeling studies have been conducted in the Alps, focusing on the LGM. Becker et al. (2016) and Seguinot et al. (2018) used a positive day-degree (PDD) model to parametrize the mass balance, and PISM, a hybrid model combining the shallow ice approximation (SIA; Hutter, 1983) with the shallow shelf approximation (SSA; Morland, 1987), to model ice flow. Cohen et al. (2017) focused their analysis on the Rhine glacier, modeled the full set of momentum equations for viscous fluids using Elmer/Ice (Gagliardini et al., 2013) and parametrized the mass balance as a linear function of surface elevation relative to the equilibrium line altitude. Although modelling studies used a variety of models and parametrizations, they all report a mismatch ranging from 500 m to over 800 m between the modeled ice thickness and geomorphological reconstructions. The reason could be difficulties in assessing the elevation of the ice surface increasing with distance from the mapped trimlines, therefore underestimating the ice thickness in the geomorphological reconstructions. Concerning the modeling, the use of present-day bedrock with or without removal of ice cover and post-glacial sediments, the difficulty to correctly simulate climate patterns in mass balance, the parametrization of ice flow, and spatial variations in timing of the LGM could in part explain the observed mismatch.

In this paper, our objective is to reconstruct the position and spatial variation of the ELA across the Alps during the LGM using a new inverse method (Višnjević et al., 2018) and the mapped ice extent during the LGM (Ehlers et al., 2011). The idea of using ELAs to gain insight into past climate patterns is not new (Callendar et al., 1950). The ELA depends primarily on two climatic variables, precipitation and temperature, which represent the effects of accumulation and ablation, respectively, and, to a lesser extent, radiation (e.g., Ohmura et al., 1992; Oerlemans, 1992). The method introduced by Višnjević et al. (2018) enables us to invert ice extent data for the reconstruction of spatial ELA variations at the scale of a mountain range like the Alps. The model assumes the ice cap to be in a steady state, with the ice sheet in near-equilibrium with climate, a scenario that has been proposed for the LGM (Clark et al., 2009; Monegato et al., 2017). We input the mapped ice extent data as the only climatic constraint because of the above mentioned uncertainties in reconstructed ice thickness. In order to reduce the calculation time, all of the codes are accelerated using graphic card units (GPUs).

Below, we start by explaining the forward ice flow model and the inversion of ice extent for the ELA reconstruction. We then review the topographic data and ice extent used. We perform a series of inverse model runs with different parameter settings to investigate the sensitivity of the results to the mass balance parameters (mass balance gradient and maximum accumulation rate), the inverse model parameters (initial guess, smoothing, update parameters), ice dynamics (deformation, sliding parameter and constriction factor), flexure (elastic thickness) and bedrock topography. We continue with reporting and interpreting the results and eventually exploit the reconstructed ELA pattern to further constrain the Alpine climate during the LGM.

2. Methods

In this section, we summarize the implementation of the forward and the inverse models. Further details can be found in Višnjević et al. (2018). For this study, we added flexural isostasy, a constriction factor for ice flow (Braun et al., 1999), spatially variable sliding and a damping factor to the forward model.

2.1. Forward model implementation

The ice flow model used, presented in Višnjević et al. (2018), is based on the shallow ice approximation (SIA) (Hutter, 1983) and solves the mass conservation equation:

$$\frac{\partial H}{\partial t} = -\nabla \cdot \mathbf{q} + b, \tag{1}$$

where H is the ice thickness and $\mathbf{q}$ is the horizontal ice flux defined as the vertically integrated velocity field. Velocities are approximated using SIA. The mass balance rate, b, is defined as:

$$b = \min(\beta(S(x, y) - ELA(x, y)), c), \tag{2}$$

where S is the ice surface, β is the mass balance gradient and c is the maximum accumulation rate. Compared to the version of the code presented in Višnjević et al. (2018), we have added flexural isostasy (Watts, 2001), assuming constant elastic properties and crustal thickness. We further implemented a constriction factor which scales ice velocity depending on cross-sectional curvature of the glacier bed to account for the effect of lateral drag not included in SIA (Braun et al., 1999; Herman and Braun, 2008; Egholm and others, 2011). Sliding is kept constant everywhere except in the accumulation zone where we calculate a 1D analytical solution for basal temperature, T_b, (Robin, 1955; Braun et al., 1999; Herman and Braun, 2008; Cohen et al., 2017) to mimic frozen bed conditions by reducing sliding in areas where T_b is below zero. Basal temperature, T_b, is calculated as:

$$T_b = T_s + \left(\frac{q}{k}\right)\sqrt{\frac{\pi H \kappa}{2b}}\mathrm{erf}\left[\sqrt{\frac{Hb}{2\kappa}}\right], \tag{3}$$

where κ is the thermal diffusivity of ice, k is the thermal conductivity of the underlying bedrock, q is the surface heat flow and H is the ice thickness. The surface temperature T_s is defined as:

$$T_s = \left(\frac{\partial T_s}{\partial z}\right)_S (S(x,y) - ELA(x,y)), \tag{4}$$

with the surface temperature gradient $(\frac{\partial T_s}{\partial z})_S$ set to constant. Where T_b is smaller than zero, the sliding parameter is adjusted. To avoid large variations at the transition between sliding and frozen-bed, we define the sliding parameter, A_s, as follows:

$$A_s = \begin{cases} f_s \cdot \max(1 + \frac{2}{3} \arctan{(T_b)}, 0.001); & \text{for } M < 0 \text{ and } T_b < 0 \\ f_s & \end{cases}. \quad (5)$$

The range of A_s goes from f_s for positive T_b, down to the minimum of 0.1% of f_s, where f_s equals $5.7{\cdot}10^{-20}$ $\mathrm{Pa^{-3}m^2s^{-1}}$ (Budd and others, 1979). A_s is updated every 100 forward model iteration steps to maintain computational performance.

Flexural isostasy is implemented using a Fourier transform solution following (Watts, 2001). To speed-up the calculation, flexure is calculated in the forward model every 1000 iterations, which corresponds to centennial or decennial updates in real time, depending on the time step. Each iteration consists of calculating diffusivity and updating ice thickness H using the mass conservation equation. The updated ice thickness represents the load in the flexure calculation. In order to calculate the full response to the load, we set the size of the Fourier domain 10 times larger than the domain of interest. In the case of the Alps, where the ice flow model calculations are computed on a 1024x1024 grid, we copy that domain to the center of a 10240x10240 grid, for which we calculate the deflection (Watts, 2001). We update the bedrock topography B with deflection and recompute all variables which depend on bedrock values, such as diffusivity, constriction factor and flux calculations. The changed bedrock topography is used to update surface altitude S and corresponding mass balance rate b (Eq. (2)).

Finally, to reduce the number of iterations needed to reach steady state, we also introduce a damping factor into the mass conservation equation following the second-order Richardson iteration method (Frankel, 1950). While iteratively updating the ice thickness, we add an additional percentage of the update from the previous iteration step, resulting in a significantly faster convergence rate.

2.2. Inversion

A detailed description of the inverse model algorithm can be found in Višnjević et al. (2018). Its objective is to invert ice extent data into a spatially varying and smooth ELA. We run the ice flow model until steady state. After each run, we compare the calculated ice extent with the one from observations (Ehlers et al., 2011) and use this comparison to update the ELA (Višnjević et al., 2018). Note that for each inversion iteration, the convergence of the forward model is the most expensive part. To reduce the convergence time needed for the forward model to reach steady state, we use the calculated ice thickness (H) of the previous inversion iteration step as a starting point for our forward model. This significantly improves the convergence of the forward model for sufficiently small changes in ELA between two iterations. The inversion algorithm starts from an initial guess for ELA (E_0) and relies mainly on the number of diffusion iterations (n_{sm}) and two parameters (τ_1 and τ_2) that together define the amplitude and amount of smoothing of the final solution. These parameters will be varied in the following sections.

Table 1: *Forward model parameter values kept constant in all scenarios*

	Constants	**Value**	**Units**
N	Max. number of inverse iterations	1000	
n_x	Number of points in x	1024	
n_y	Number of points in y	1024	
dx	Spatial resolution in x	784.5	m
dy	Spatial resolution in y	568.4	m
ρ	Ice density	910	kgm^{-3}
g	Gravitational constant	9.81	ms^{-2}
n	Exponent in Glen flow law	568.4	m
A	Deformation parameter	$1.9 \cdot 10^{-24}$	$Pa^{-3}s^{-1}$
f_s	Sliding parameter	$5.7 \cdot 10^{-20}$	$Pa^{-3}s^{-1}$
yr	Seconds per year	31556926	s
c_{stab}	Time step coefficient	0.1235	
q	surface heat flow	$70 \cdot 10^{-3}$	mWm^{-2}
k	Thermal conductivity of underlying bedrock	2.35	$Wm^{-1}K^{-1}$
$(\frac{\partial T}{\partial z})_S$	Surface temperature gradient	0.005	$°Cm^{-1}$
κ	Thermal diffusivity of ice	2.35	m^2s^{-1}
ρ_a	Asthenosphere density	3300	kgm^{-3}
ν	Poissons ratio	0.25	
Y_m	Youngs module	568.4	Pa

3. Data

Bedrock topography, ice extent and mass balance rate parameters (maximum accumulation rate c and mass balance gradient β, (Eq. 2)), are needed as input for our calculations. We use SRTM data (Jarvis and others, 2008) as bedrock topography, where present day ice cover and post-glacial sediments are included. To test how changes in bedrock topography influence the result (Fig. 8), we run our model on the bedrock topography provided by Mey et al. (2016), from which the sediment fill has been removed based on a neural network approach. The LGM ice extent used is a simplified version of the ice extent from Ehlers et al. (2011) (Fig. 1). The mapped ice extent was simplified because of difficulties with fitting the modeled ice extent to the original south-western border, where only valley glaciers have been mapped and the highest parts of the landscape appear ice free. To test the influence of the mass balance rate parameters on the inversion result we choose a range of values for the maximum accumulation rate c (Table 2) representing drier conditions over the Alps reported from both data (pollen) and numerical studies (Peyron et al., 1998; Cohen et al., 2017). The range of values tested for c matches the one from Cohen et al. (2017), where c in their driest and wettest scenarios equals 0.26 m/yr and 1.80 m/yr, respectively. Mass balance gradient β was tested for a larger range of values than reported in other studies (Huss et al., 2008; Cohen et al., 2017), in order to explore potentially different climatic scenarios. Following Huss et al. (2008), typical β for alpine glaciers in the accumulation zone would be 0.009 a^{-1}, and 0.005 a^{-1} in the ablation zone. Although different values for β have been observed in the accumulation and the ablation zone (Mayo, 1984; Huss et al., 2008), and used in modeling studies (Cohen et al., 2017), we keep it constant throughout the ice cap for simplicity in this study.

Glaciation of the Alps during the LGM will also have an impact on topography due to an isostatic effect. The additional load of the large and heavy ice mass bends the lithospheric plate, lowering topography. Removal of that ice during deglaciation results in slow but measurable uplift of the topography. It has recently been argued that most of the currently observed uplift is inherited from the rapid melting of the LGM ice cap (Mey et al., 2016), although this is still a subject of discussion (Sternai et al., 2019). Others argue that up to 60% of this uplift is due to erosion (Champagnac et al., 2007). For our purpose, we must calculate the deflection of the lithosphere and therefore know the elastic thickness of the lithosphere. Unfortunately, estimates vary from 7 to 70 km (Champagnac et al., 2007; Sternai et al., 2013; Mey et al., 2016). In any case, the maximum deflection ranges from 100 m to 280 m, depending on the value for the elastic thickness used (Mey et al., 2016), which is only a fraction of the relief of the Alps.

4. Results

In this section, we report inversion results for 25 different scenarios. To investigate the robustness of the solution, we explore the parameter space of both the inverse and the forward model parameters. Below, four categories

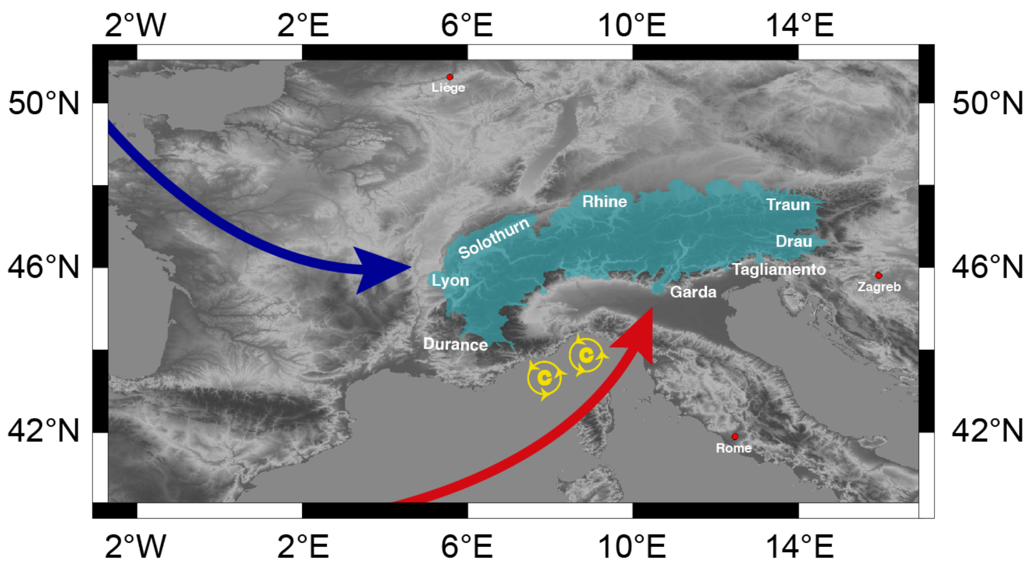

Figure 1: Schematic representation of the debated climatic regimes dominating Alpine climate during the LGM: zonal atmospheric circulation (blue) (Peyron et al., 1998), meridional (southern) circulation (red) (Florineth and Schlüchter, 2000), more frequent cyclone generation in the Gulf of Genoa (yellow) (Kuhlemann et al., 2008). Ice extent (green) used as input for the inversion.

of experiments are presented. We vary (1) the climate variables, (2) the inverse model parameters, (3) the ice flow parameters and (4) the geodynamic properties. To investigate the role of climate, we vary parameters defining the mass balance rate, i.e., the maximum accumulation rate c (Fig. 2) and the mass balance gradient β (Fig. 3). For the inverse parameters, we test the influence of the initial guess on the solution (Fig. 4), the influence of smoothing (Figs. 5A and 5B) through the update parameters, i.e., τ_1 and τ_2 (Figs. 5C and 5D). To assess the role of ice mechanics, we vary the deformation parameter A (Figs. 6A and 6B), maximum value for the sliding parameter A_s (Figs. 6C and 6D) and the constriction factor Γ (Figs. 6E and 6F). Finally, the influence of geodynamic properties is investigated by varying the elastic thickness (Fig. 7) as well as the effect of bedrock topography (Fig. 8). Parameters kept constant in all scenarios can be found in Table 1. The list of parameters and the range of tested values can be found in Table 2. The underlined values in Table 2 are used unless stated differently in the text. Note that only one parameter is varied at a time.

A common feature in our results is a clear W-E gradient in ELA from the Lyon region to the east of Traun. The N-S gradient is less clear, it is more pronounced in the west (Solothurn lobe - Durance glacier) and the center of the Alps (Rhine glacier - Garda glacier), while in the east (Traun glacier - Drau glacier) it cannot be seen. In the center of the Alps, the gradient is tilted going from NW to SE, from the Rhine glacier towards the broader Garda glacier. In all scenarios, the ELA may be overestimated in the SW

Table 2: *List of parameters and a range of values varied in the result*

	Parameters	**Tested values**					**Units**
c	Max accumulation rate	0.25	0.5	$\underline{1.0}$	2.0		myr^{-1}
β	Mass balance gradient	0.0015	$\underline{0.004}$	0.007	0.01	0.015	a^{-1}
A	Deformation parameter	$0.25 \cdot \mathrm{A}$	$\underline{\mathrm{A}}$	$3 \cdot \mathrm{A}$			$\mathrm{Pa}^{-3}\mathrm{s}^{-1}$
$\mathrm{f_s}$	Sliding parameter	$0.25 \cdot \mathrm{f_s}$	$\underline{\mathrm{f_s}}$	$3 \cdot \mathrm{f_s}$			$\mathrm{Pa}^{-3}\mathrm{s}^{-1}$
Γ	Constriction factor	500	$\underline{2000}$	4000			
$\mathrm{T_e}$	Elastic thickness	10	$\underline{30}$	50			km
$\mathrm{E_0}$	Initial guess	$\underline{1400}$	1900				m
$\mathrm{n_{sm}}$	Number of diffusion iter	40	$\underline{400}$	4000			
τ_1	Inversion update param	$\underline{45}$	500				m
τ_2	Diffusion update param	$0.1 \cdot \mathrm{dy}^2$	$\underline{0.25 \cdot \mathrm{dy}^2}$				m^2

region of the ice extent where it is significantly higher than in the rest of the mountain range, due to complex topography in the region and our simple approximation of the ice flow.

4.1. Sensitivity to climate (mass balance rate parameters: β, c)

To investigate the role of climate in our model (Eq. (2)), we vary the maximum accumulation rate, c, and the mass balance gradient, β. The initial ELA for all of the scenarios within this subsection is set to 1400 m. If not varied in the scenario, β was set to 0.004 a^{-1} and c was set to 0.5 m/yr. All the results took 1000 inverse model iterations, except for scenarios presented in Figs. 2A and 2B where it took 750 and 900 iterations, respectively.

The maximum accumulation rate, c, corresponds to the maximum amount of ice accumulated within a year. A larger value for c prescribes wetter conditions over the Alps, while a lower c means a more arid climate (Eq. (2)). Fig. 2 depicts the inversion model results for scenarios with different c,

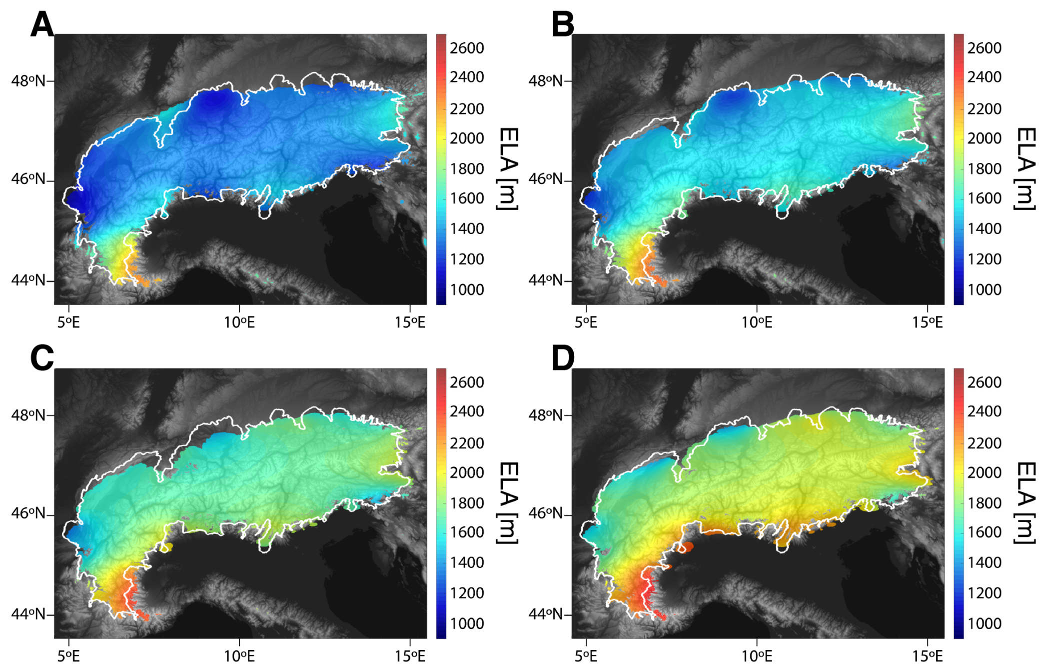

Figure 2: Influence of the maximum accumulation rate c on the modeled ELA field. Results are presented where there is ice, bedrock elevation is depicted in gray, white outline represents mapped LGM extent. (A) c = 0.25 m/yr, (B) c = 0.5 m/yr, (C) c = 1.0 m/yr, (D) c = 2.0 m/yr.

0.25 m/yr (Fig. 2A), 0.5 m/yr (Fig. 2B), 1.0 m/yr (Fig. 2C) and 2.0 m/yr (Fig. 2D). Higher values for c have not been tested as they would imply significantly wetter conditions than reported for the Alps during the LGM (Peyron et al., 1998; Cohen et al., 2017). Fig. 2 shows that the ELA rises as c increases. This is because a larger c leads to thicker ice and therefore a more elevated ice surface and a larger ice cap. By raising the ELA, the ablation zone is enlarged and the modeled ice extent fits the observations.

The results reveal a W-E gradient in ELA, ranging from 1000 m - 1550 m in the west near Lyon to 1650 m - 2000 m east of Traun and north of Drau. In the central part of the Alps the N-S gradient in ELA ranges from about 1120 m - 1500 m near the Rhine glacier to 1500 m - 2150 m in the broader Garda region. In the west the N-S gradient (Solothurn lobe - Durance glacier) is more pronounced, ranging from 1350 m - 1500 m in the north to 1750 m - 2000 m near the Durance glacier and a maximum values of 2200 m - 2450 m in the southernmost part of the Alps.

We investigate the role of the mass balance gradient β for values ranging from 0.0015 to 0.015 a^{-1} (Table 2). The results are shown in Figure 3. The position of the ELA decreases as β increases. This is because β not only determines the elevation above ELA at which the mass balance rate reaches the maximum accumulation value c (Eq. (2)), but also has a strong control on the rate at which the glacier ablates. A lower β means a gradual change in b with altitude, and corresponds to dry (sub)arctic conditions, while a higher β implies a steep change in b and corresponds to extreme maritime climate conditions (Oerlemans and Fortuin, 1992). Reported drier conditions over the Alps during the LGM (Peyron et al., 1998; Florineth and Schlüchter, 2000) would favour lower β values. The W-E and N-S gradients in ELA discussed above remain regardless of the β used (Figs. 3 and 2B (β 0.004 a^{-1})).

4.2. Sensitivity to the inverse model parameters

We investigate the influence of the inverse model parameters on the inversion results by changing the initial guess (Fig. 4), smoothing n_{sm} (Figs. 5A and

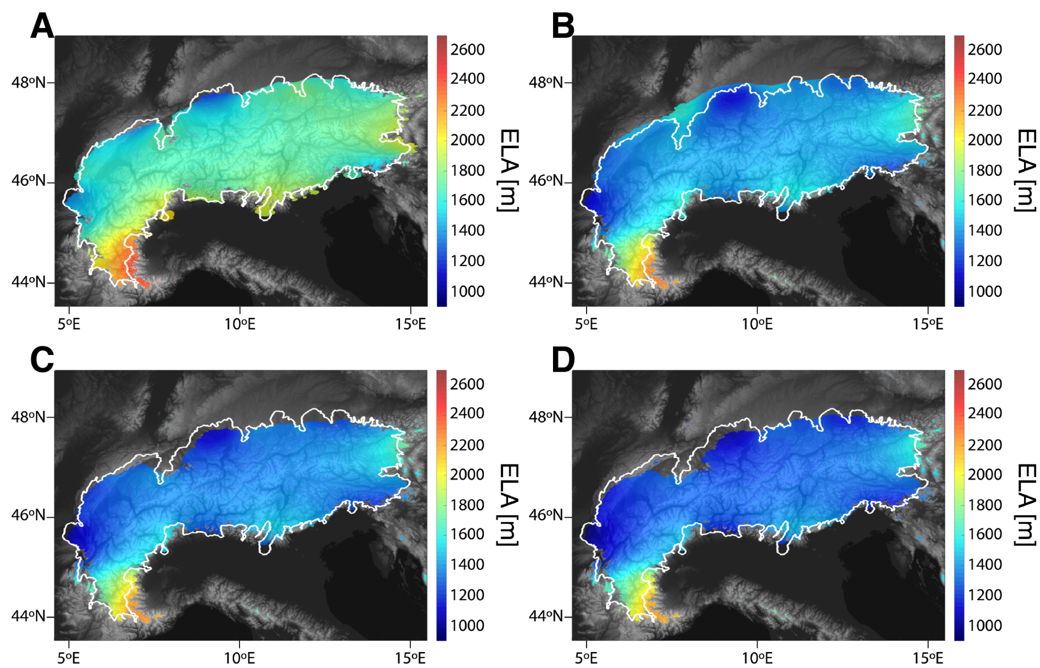

Figure 3: Influence of the mass balance gradient β on the modeled E field. Results are presented where there is ice, bedrock elevation is depicted in gray, white outline represents mapped LGM extent. (A) β is set to 0.0015 a^{-1}, (B) β is set to 0. 007 a^{-1}, (C) β is set to 0.01 a^{-1}, (D) β is set to 0.015 a^{-1}.

5B) and the update parameters, τ_1 and τ_2 (Figs. 5C and 5D).

The influence of the initial guess E_0, i.e., the initial value of the ELA, is tested in two climate scenarios (Fig. 4). For each climate scenario, results are presented for two different initial guess values, 1400 m and 1900 m. In the first case (Scenario A) the maximum accumulation rate, c, was set to 1 m/yr and β to 0.004 a^{-1} (4A and 4B), while in the second case (Scenario B) c was set to 0.5 m/yr and β to 0.01 a^{-1} (Figs. 4C and 4D). Both scenarios show very small or no influence of the initial guess on the result. While Figs. 4A and 4B show no difference in the resulting ELA fields, Figs. 4C and 4D show small local differences in ice cover between two scenarios with the described gradients remaining.

The influence of the number of diffusion iterations, which control the amount of smoothing in the resulting ELA field, is visualized in Figs. 5A and 5B. We present two end-member scenarios with 40 and 4000 iterations. A small number of iterations fits the edges of the ice extent more precisely, introducing local variations to the ELA field (Fig. 5A). A large number of iterations removes the local variations. In all results the W-E and the N-S gradients in the ELA field (Fig. 5B) are preserved. This indicates that the two major gradients in the ELA field do not emerge due to local phenomena.

The inversion update parameters τ_1, the amplitude of the ELA update, and τ_2, the amplitude of the applied smoothing, also influence the variance of the resulting ELA field. A large τ_1, i.e., 500 (Fig. 5C), leads to large variations in ELA on the edges of the ice extent, overemphasising local variations.

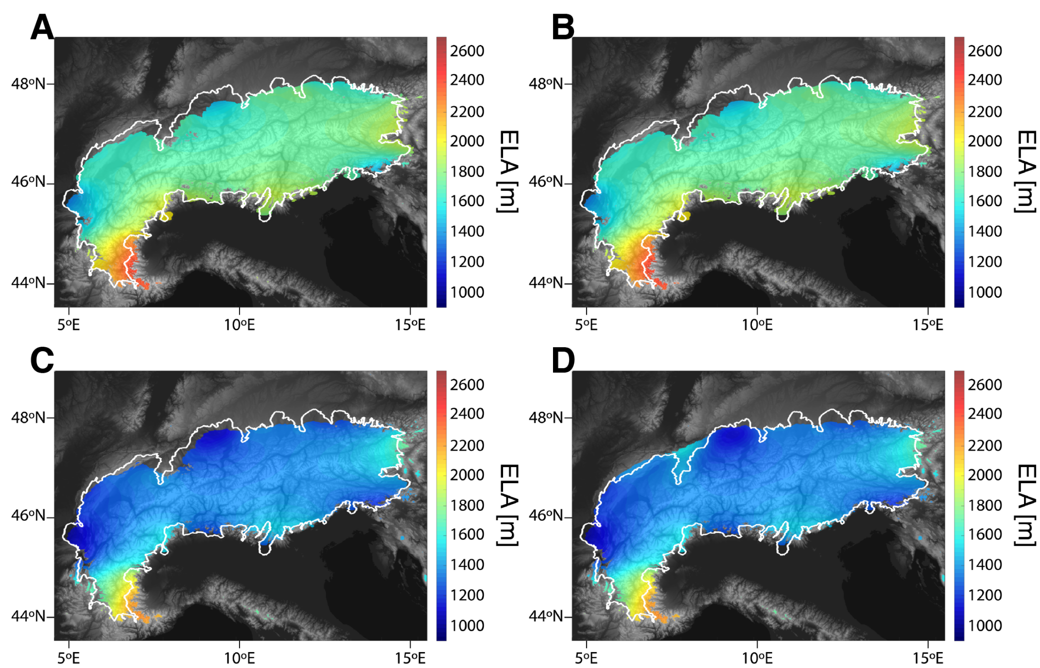

Figure 4: Modeled ELA fields for different initial guesses of the ELA for Scenario A and B described in section 4.2. (A) Scenario A with initial guess set to 1400 m, (B) Scenario A with initial guess set to 1900 m, (C) Scenario B with initial guess set to 1400 m, (D) Scenario B with initial guess set to 1900 m. Results are presented where there is ice, bedrock elevation is depicted in gray, white outline represents mapped LGM extent.

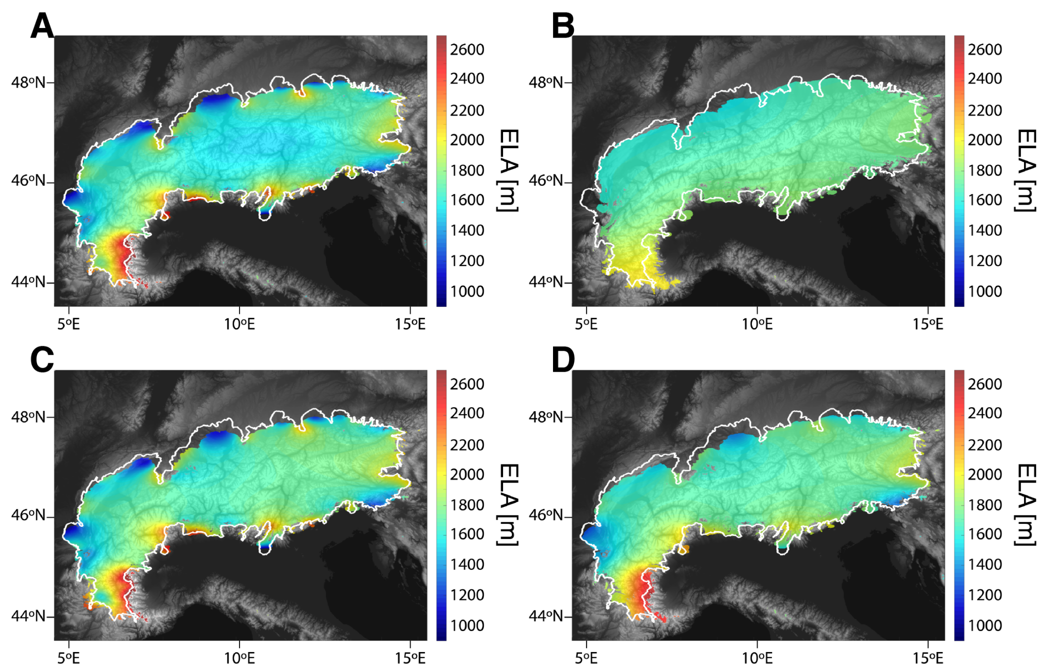

Figure 5: Influence of smoothing on the modeled ELA field. Results are presented where there is ice, bedrock elevation is depicted in gray, white outline represents mapped LGM extent. (A) Number of smoothing iterations is set to 40. (B) number of smoothing iterations is set to 4000, (C) τ_1 is set to 500, (D) τ_2 is set to $0.01{\cdot}\mathrm{dy}^2$.

Note that these differences are maintained during the iterative process, which prevents the algorithm to converge. A result for τ_1 much smaller than the standard value of 45 is not presented because very small changes in ELA between two iterations do not lead to a difference in the resulting ice extent. A smaller value of τ_2, set to 0.1dy^2 (Fig. 5D), reduces the influence of smoothing between two iterations, this in turn increases the number of iterations for the inverse model to converge. Besides changing the value of inverse parameters, the scenarios presented in Fig. 5 are the same as in Fig. 4A (c set to 1 m/yr and β to 0.004 a^{-1}).

4.3. Sensitivity to ice mechanics (deformation parameter, sliding parameter, constriction factor)

The tested ice mechanics scenarios consist of varying the deformation parameter A (Table 1), between $0.25A$ and $3A$ (Figs. 6A and 6B), the sliding parameter A_s, between $0.25A_s$ and $3A_s$ (Figs. 6C and 6D) and the constriction factor Γ, between 500 and 4000 (Figs. 6E and 6F). The initial ELA for each of the scenarios was 1900 m, β was set to 0.004 a^{-1} and c was set to 1 m/yr. Results for this scenario but with underlined values from Table 2 used for A, A_s and Γ are depicted in Fig. 2C. It is important to keep in mind that the SIA forward model is not solving a full set of Stokes equations and is only a rough approximation of ice flow. This implies that the complete parameter space and the role of ice mechanics is not fully explored here. The objective is simply to test the robustness of the inversion results, and seek for common characteristics between inversion results. Presented results took 1000 inverse model iterations, except for scenarios presented in Figs. 6C and 6D where it took 600 iterations.

First, we test the role of the deformation factor on the solution. In Figs. 6A and 6B, we show the solutions for different A values. Reducing the deformation parameter leads to thicker ice, which leads to a higher ELA. Figs. 6C and 6D show the results for varying the maximum value of the sliding parameter. While we varied deformation and sliding parameters in the same way, one quarter and three times the values used in Fig. 2C, Fig. 6 shows that the inversion result is significantly more sensitive to changes of the deformation parameter than the sliding parameter. The role of the constriction factor is investigated in Figs. 6E and 6F, showing little to no change in the results (Fig. 6).

4.4. Sensitivity to elastic thickness

To investigate the role of flexure we vary the elastic thickness T_e. Although it is known that the elastic thickness under the Alps varies in space (Mey et al., 2016) we keep it spatially uniform and test two end member scenarios for $T_e = 10$ km and $T_e = 50$ km. The initial guess for the ELA for both scenarios was 1900 m, β was set to 0.004 a^{-1} and c was set to 1 m/yr. Fig. 7 shows negligible differences between the two solutions. It seems that on this scale, the change in elastic thickness does not influence the Alpine ice cap enough to change the final result of the inversion.

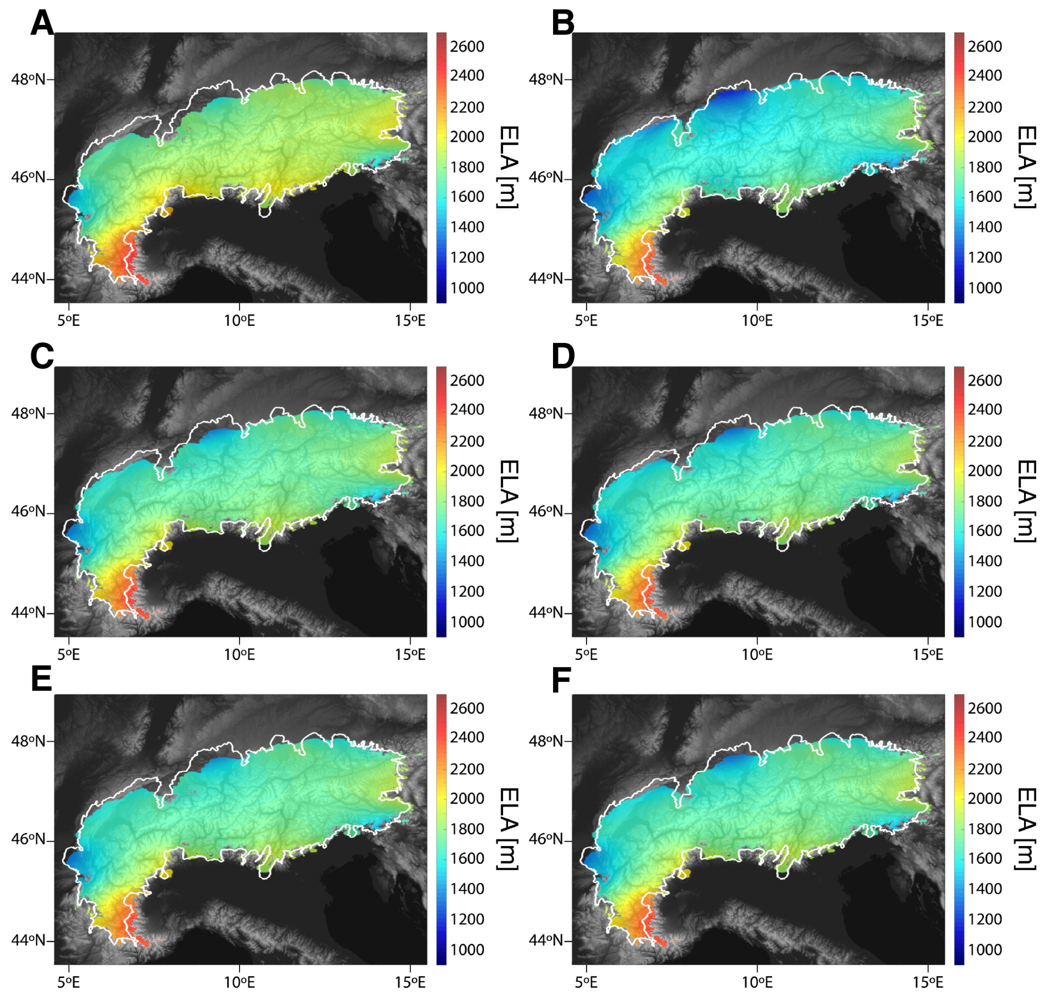

Figure 6: Influence of ice mechanics on the modeled ELA field. Results are presented where there is ice, bedrock elevation is depicted in gray, white outline represents mapped LGM extent. (A) Value of A is 0.25 times smaller than reported in Table 1, (B) value of A is three times larger than reported in Table 1, (C) Maximum value of A_s is 0.25 times smaller than reported in Table 1, (D) Maximum value of A_s is three times larger than reported in Table 1., (E) Γ is set to 500, (F) Γ is set to 4000.

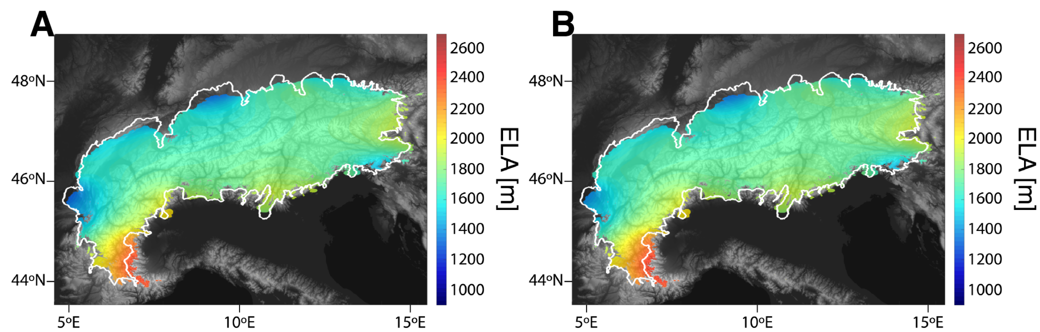

Figure 7: Influence of elastic thickness T_e on the modeled ELA field. Results are presented where there is ice, bedrock elevation is depicted in gray, white outline represents mapped LGM extent. (a) T_e is set to 10 km, (b) T_e is set to 50 km.

4.5. Sensitivity to bedrock topography

Finally, we test the influence of bedrock topography on the inversion results. To test this we use a bedrock topography with removed post-LGM valley fills created by Mey et al. (2016). The setup is the same as for Fig. 2C, with an initial guess of 1400 m, β set to 0.004 a^{-1} and c set to 1 m/yr. Fig. 8 shows no difference between this result and the ones using present day topography as bedrock. The calculated ice thickness is higher in the areas where the sediment has been removed but that does not influence the ice surface, therefore not changing the result significantly. This implies that our method can yield useful information on past environments even when applied to present-day topography.

5. Discussion

The aim of this paper is to estimate the mass balance rate in the Alps during the LGM and how it varies in space using the inverse method described in

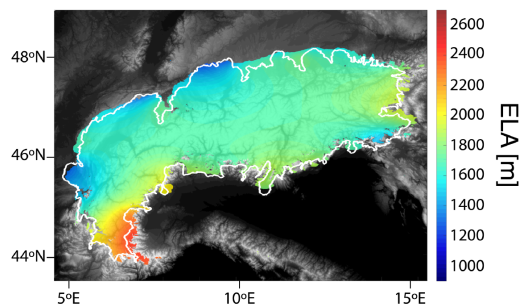

Figure 8: Influence of bedrock topography on the modeled ELA field. Bedrock from Mey et al. (2016) was used in the presented scenario. Results are presented where there is ice, bedrock elevation is depicted in gray, white outline represents mapped LGM extent.

Višnjević et al. (2018). We report a series of inverse results that highlight spatial variations in the position of the equilibrium line altitude (ELA), and thus mass balance rate. To evaluate the robustness of our results, we ran a series of experiments in which we test the influence of the mass balance parameters, the inverse parameters, the ice dynamics, the flexural rigidity and variations in bedrock topography on the inferred equilibrium line altitude.

The most robust feature we observe is the presence of a W-E gradient in ELA across the Alps, with the position of the equilibrium line raising eastward. Such a gradient may imply higher precipitation in the western parts of the Alps compared to the east. As the air is lifted across the Alps, the air dries out and the equilibrium line altitude raises. Such an eastward flow supports the idea of zonal circulation-dominated conditions during the LGM (Peyron et al., 1998), and therefore precludes the idea of having meridional-dominated precipitation during the LGM (Florineth and Schlüchter, 2000). Interestingly, the need for a W-E gradient in the position of the equilibrium line altitude was also found by a recent and independent study (Seguinot et al., 2018), in which the authors modeled the transient evolution of the Alpine ice cap over a full glacial cycle (120-0 ka).

The second feature common to most inversion results is the presence of a N-S gradient in the western and central Alps, with the equilibrium line altitude rising from north to south, that is contrasted with the absence of a N-S gradient in the eastern Alps. One may think that the N-S gradient observed simply results from a temperature increase towards lower latitudes. However, assuming a standard latitudinal temperature lapse rate of 0.7°C per 1° of latitude (La Sorte et al., 2014) and a 6.5°C/km ELA lapse rate (Kuhlemann et al., 2008) suggests a difference in equilibrium line altitude across the LGM ice cap of about 240 m in the central Alps and of about 340 m in the western Alps. The gradient predicted by our inversion in the western and central Alps is systematically larger; $\sim$400 m in the center and between 360 and 510 m in the west. Therefore, we speculate that other mechanisms than latitudinal temperature gradients must be invoked. In the western and central Alps, the inferred enhanced N-S gradient may be explained by an orographic precipitation pattern, i.e. higher precipitation rates on the northern flanks of the Alps compared to the south. Such a precipitation pattern would again imply zonal circulation-dominated conditions. Explaining the absence of a N-S gradient in the eastern Alps is, however, more complicated, and could be reflecting the influence of local conditions, such as strongly enhanced precipitation in the Tagliamento region and the north Adriatic sea, as can be seen in the present day annual precipitation pattern (Isotta and others, 2014; Mey et al., 2016, Supplementary Figure 5). A local increase in precipitation in the SE would lead to a regionally lower ELA, obscuring the N-S gradient in the eastern Alps.

Our approach does not enable us to constrain the absolute position of the equilibrium line altitude. The equilibrium line altitude depends on both precipitation and temperature (Ohmura et al., 1992), which cannot be disentangled using the ice extent alone. While changes in temperature primarily lead to changes in the position of the equilibrium line altitude (e.g., Oerlemans, 1997), changes in precipitation and humidity are primarily reflected by changes in the maximum accumulation rate c and the mass balance rate gradient β. An increase in the maximum accumulation rate c means an increase in precipitation rate, while an increase in β reflects an increase in humidity (Oerlemans and Fortuin, 1992; Ohmura et al., 1992). Higher accumulation rates generate thicker ice caps and higher ice fluxes, with the implication that a higher c requires a higher equilibrium line altitudes for the same ice extent (Fig. 2). In contrast, increasing β induces larger ablation rates (Fig. 3), which must be compensated by a lowering of the equilibrium line altitude. As a result, large variations can be observed in the position of the equilibrium line altitude depending on the choice of c and β. Although, low c and β would correspond to drier conditions during the LGM, as suggested by field studies (Peyron et al., 1998), they can unfortunately not be constrained directly.

A clear limitation of our study is the assumption of spatially uniform c and β, so any spatial variations in precipitation will be reflected by a change in the position of the equilibrium line altitude. Recently, Mey et al. (2016) used a spatially variable c calibrated using modern annual precipitation data. Although the model predicts similar equilibrium line altitude patterns to ours, differences in absolute values can easily be explained by different c and β. Similarly, Becker et al. (2016) used a steady state model but included a reduction in precipitation north of the weather divide to reproduce the observed LGM ice extent, which they interpreted to reflect a reduction in precipitation rate on the northern flanks of the Alps due to a southward shift of the dominating storm track. However, they did not investigate how the equilibrium line altitude varies from west to east, which is one of our main findings.

Another limitation of our study is the steady state assumption of the ice extent at the LGM. Seguinot et al. (2018) argued that the LGM extent was a transient stage, concluding that there was a disequilibrium between glaciers and climate throughout the period. This implies that the timing of extent could be different in the north compared to the south. Unfortunately, we do not know how far the LGM climate was from the steady state assumption, while uncertainties of available dating techniques make it difficult to precisely identify asynchronous ice extents in time and space. In our model, it takes only about 1000 years for the ice cap to grow to the observed LGM extent and closely approach a climatic steady state. In a theoretical study Herman et al. (2018) report response times of a glacier on a similar time scale. These response times to climatic perturbations are shorter than the duration of the LGM (Clark et al., 2009). Furthermore, we observe large LGM moraines at the glacier outlets, implying longer periods of stability. For these reasons, it seems possible that the Alpine ice cap was in its position and close to steady state during most of the LGM.

Compared to the present day ELA with a mean of around 3000 m (Huss et al., 2008), our reconstructions show an overall decrease of about 1200 m to 1700 m for the LGM. Assuming that the change in equilibrium line altitude is solely due to temperature and using the same temperature - ELA relation as above, we arrive at a temperature depression of 7.8°C - 11°C, which falls in the range of values reported from modeling studies (Jost et al., 2005; Kageyama et al., 2006), compared to 12±3°C mean annual temperature depression inferred from pollen (Peyron et al., 1998). This would imply a strong temperature control on the equilibrium line altitude. These results, however, must be treated with caution, as temperature cannot be determined independently.

6. Conclusion

We reconstructed the spatially variable altitude of the equilibrium line over the Alps during the LGM, following the inverse modelling approach described in Višnjević et al. (2018). Ice extent data from Ehlers et al. (2011) and a DEM of the Alps are used as input data for the model. We have conducted sensitivity tests for both the inverse and forward model parameters. Our model can reproduce the mapped LGM ice extent for a range of climatic scenarios, resulting in different ELA fields but keeping a distinct spatial pattern. The modeled ELA fields of the Alps are dominated by a W-E gradient, regardless of the chosen scenario. A pronounced N-S gradient can also be observed across scenarios in the central and western part of the mountain range. However, the absence of a pronounced N-S gradient in ELA over the entire Alps precludes the hypothesis of a southward shift of the westerlies during the LGM.

Acknowledgments

VV was funded through SNF grant CRSII_2154434. The authors would like to thank J. Mey for providing us with the bedrock map with removed sediment fill. Thanks to N. Stalder, J. Elkadi and B. Lehmann for discussions.

References

Becker P., Seguinot J., Jouvet G. and Funk M. (2016) Last Glacial Maximum precipitation pattern in the Alps inferred from glacier modelling. *Geographica Helvetica*, 71(3), pp.173-187.

Bini, A., Buoncristiani, J., Couterrand, S., Ellwanger, D., Felber, M., Florineth, D., Graf, H., Keller, O., Kelly, M., Schlüchter, C. and Schoeneich, P. (2009) Die Schweiz während des letzteiszeitlichen Maximums (LGM). *Bundesamt für Landestopografie swisstopo.*

Braun, J., Zwartz, D. and Tomkin, J.H. (1999) A new surface-processes model combining glacial and fluvial erosion. *Annals of Glaciology*, 28, pp.282-290.

Budd W.E., Keage P.L. and Blundy N.A. (1979) Empirical studies of ice sliding. *Journal of Glaciology* 23(89), 157-170.

Callendar, G.S. (1950) Note on the relation between the height of the firn line and the dimensions of a glacier. *Journal of Glaciology*, 1(8), pp.459-461.

Champagnac, J.D., Molnar, P., Anderson, R.S., Sue, C. and Delacou, B. (2007) Quaternary erosion-induced isostatic rebound in the western Alps *Geology*, 35(3), pp.195-198.

Clark, P.U., Dyke, A.S., Shakun, J.D., Carlson, A.E., Clark, J., Wohlfarth, B., Mitrovica, J.X., Hostetler, S.W. and McCabe, A.M. (2009) The last glacial maximum. *Science*, 325(5941), pp.710-714.

Cohen, D., Gillet-Chaulet, F., Haeberli, W., Machguth, H. and Fischer, U.H. (2017) Numerical reconstructions of the flow and basal conditions of the Rhine glacier, European Central Alps, at the Last Glacial Maximum. *The Cryosphere*, 12(8), pp.2515-2544.

Egholm D.L., Knudsen M.F., Clark C.D. and Lesemann J.E. (2011) Modeling the flow of glaciers in steep terrains: The integrated second-order shallow ice approximation (iSOSIA). *Journal of Geophysical Research: Earth Surface*, 116(F2).

Ehlers, J., Gibbard, P.L. and Hughes, P.D. eds. (2011) Quaternary glaciations-extent and chronology: a closer look. *Developments in quaternary science*, (Vol. 15). Elsevier.

Florineth, D. and Schlüchter, C. (2000) Alpine evidence for atmospheric circulation patterns in Europe during the Last Glacial Maximum. *Quaternary Research*, 4(3), pp.295-308.

Frankel, S.P. (1950) Convergence rates of iterative treatments of partial differential equations. *Mathematical Tables and Other Aids to Computation*, 4(30), pp.65-75.

Gagliardini, O., Zwinger, T., Gillet-Chaulet, F., Durand, G., Favier, L., Fleurian, B.D., Greve, R., Malinen, M., Martín, C., Råback, P. and Ruokolainen, J. (2013) Capabilities and performance of Elmer/Ice, a new-generation ice sheet model. *Geoscientific Model Development*, 6(4), pp.1299-1318.

Herman, F. and Braun, J. (2008) Evolution of the glacial landscape of the Southern Alps of New Zealand: Insights from a glacial erosion model. *Journal of Geophysical Research: Earth Surface*, 113(F2).

Herman, F., Braun, J., Deal, E. and Prasicek, G. (2018) The response time of glacial erosion. *Journal of Geophysical Research: Earth Surface* 123(4), pp.801-817.

Heyman, B.M., Heyman, J., Fickert, T. and Harbor, J.M. (2013) Paleoclimate of the central European uplands during the last glacial maximum based on glacier mass-balance modeling. *Quaternary Research*, 79(1), pp.49-54.

Hofer, D., Raible, C.C., Merz, N., Dehnert, A. and Kuhlemann, J. (2012) Simulated winter circulation types in the North Atlantic and European region for preindustrial and glacial conditions. *Geophysical Research Letters*, 39(15).

Huss, M., Bauder, A., Funk, M. and Hock, R. (2008) Determination of the seasonal mass balance of four Alpine glaciers since 1865. *Journal of Geophysical Research: Earth Surface*, 113(F1).

Hutter K. (1983) *Theoretical Glaciology.* Kluwer, Dordrecht, Holland.

Isotta, F.A., Frei, C., Weilguni, V., Perčec Tadić, M., Lassegues, P., Rudolf, B., Pavan, V., Cacciamani, C., Antolini, G., Ratto, S.M. and Munari, M. (2014) The climate of daily precipitation in the Alps: development and analysis of a highresolution grid dataset from panAlpine raingauge data. *International Journal of Climatology)*, 34(5), pp.1657-1675.

Janská, V., Jiménez-Alfaro, B., Chytrý, M., Divíšek, J., Anenkhonov, O., Korolyuk, A., Lashchinskyi, N. and Culek, M. (2017) Palaeodistribution modelling of European vegetation types at the Last Glacial Maximum using modern analogues from Siberia: Prospects and limitations. *Quaternary Science Reviews*, 159, pp.103-115.

Jarvis A., Reuter H.I., Nelson A. and Guevara E. (2008) Hole-filled SRTM for the globe Version 4. *available from the CGIAR-CSI SRTM 90m Database (http://srtm. csi. cgiar. org)*.

Jost, A., Lunt, D., Kageyama, M., Abe-Ouchi, A., Peyron, O., Valdes, P.J. and Ramstein, G. (2005) High-resolution simulations of the last glacial maximum climate over Europe: a solution to discrepancies with continental palaeoclimatic reconstructions? *Climate Dynamics*, 24(6), pp.577-590.

Jouvet G., Picasso M., Rappaz J. and Blatter H. (2008) A new algorithm to simulate the dynamics of a glacier: theory and applications. *Journal of Glaciology*, 54(188), 801-811.

Kageyama, M., Laine, A., Abe-Ouchi, A., Braconnot, P., Cortijo, E., Crucifix, M., De Vernal, A., Guiot, J., Hewitt, C.D., Kitoh, A. and Kucera, M. (2006) Last Glacial Maximum temperatures over the North Atlantic, Europe and western Siberia: a comparison between PMIP models, MARGO seasurface temperatures and pollen-based reconstructions. *Quaternary Science Reviews*, 25(17-18), pp.2082-2102.

Kessler M.A., Anderson R.S. and Stock G.M. (2006) Modeling topographic and climatic control of east-west asymmetry in Sierra Nevada glacier length during the Last Glacial Maximum. *Journal of Geophysical Research: Earth Surface* , 111(F2).

Kuhlemann, J., Rohling, E.J., Krumrei, I., Kubik, P., Ivy-Ochs, S. and Kucera, M. (2008) Regional synthesis of Mediterranean atmospheric circulation during the Last Glacial Maximum. *Science*, 321(5894), pp.1338-1340.

La Sorte, F.A., Butchart, S.H., Jetz, W. and Böhning-Gaese, K. (2014) Range-wide latitudinal and elevational temperature gradients for the world's terrestrial birds: implications under global climate change. *PloS one*, 9(5), p.e98361.

Luetscher, M., Boch, R., Sodemann, H., Spötl, C., Cheng, H., Edwards, R.L., Frisia, S., Hof, F. and Müller, W. (2015) North Atlantic storm track changes during the Last Glacial Maximum recorded by Alpine speleothems. *Nature Communications*, 6, p.6344.

Mayo LR (1984) Glacier mass balance and runoff research in the USA. *Geografiska Annaler: Series A, Physical Geography*,215-227.

Mey, J., Scherler, D., Wickert, A.D., Egholm, D.L., Tesauro, M., Schildgen, T.F. and Strecker, M.R. (2016) Glacial isostatic uplift of the European Alps. *Nature communications*, 7, p.13382.

Mikolajewicz, U. (2011) Modeling mediterranean ocean climate of the last glacial maximum. *Climate of the Past*, 7(1), pp.161-180.

Monegato, G., Scardia, G., Hajdas, I., Rizzini, F. and Piccin, A. (2017) The Alpine LGM in the boreal ice-sheets game. *Scientific Reports*, 12(10), 7(1), p.2078.

Morland, L.W. (1987) Unconfined ice-shelf flow. *Dynamics of the West Antarctic Ice Sheet* , pp. 99-116. Springer, Dordrecht.

Oerlemans J. (1992) Climate sensitivity of glaciers in southern Norway: Application of an energy-balance model to Nigardsbreen, Hellstugubreen and Alfotbreen. *Journal of Glaciology*, 38(129), 223-232.

Oerlemans, J. and Fortuin, J.P.F. (1992) Sensitivity of glaciers and small ice caps to greenhouse warming. *Science*, 258(5079), pp.115-117.

Oerlemans J. (1997) Climate sensitivity of Franz Josef Glacier, New Zealand, as revealed by numerical modeling. *Arct. Alp. Res.*, 29, 233239.

Ohmura, A., Kasser, P. and Funk, M. (1992) Climate at the equilibrium line of glaciers. *Journal of Glaciology*, 38(130), pp.397-411.

Peyron, O., Guiot, J., Cheddadi, R., Tarasov, P., Reille, M., de Beaulieu, J.L., Bottema, S. and Andrieu, V. (1998) Climatic reconstruction in Europe for 18,000 yr BP from pollen data. *Quaternary research*, 49(2), pp.183-196.

Porter, S.C. (1975) Equilibrium-line altitudes of late Quaternary glaciers in the Southern Alps, New Zealand. *Quaternary research*, 5(1), pp.27-47.

Ramstein, G., Kageyama, M., Guiot, J., Wu, H., Hly, C., Krinner, G. and Brewer, S. (2007) How cold was Europe at the Last Glacial Maximum? A synthesis of the progress achieved since the first PMIP model-data comparison. *Climate of the Past*, 3(2), pp.331-339.

Riviere, G., Laine, A., Lapeyre, G., Salas-Mlia, D. and Kageyama, M. (2010) Links between Rossby wave breaking and the North Atlantic Oscillation-Arctic Oscillation in present-day and Last Glacial Maximum climate simulations. *Journal of Climate*, 23(11), pp.2987-3008.

Robin, G.D.Q. (1955) Ice movement and temperature distribution in glaciers and ice sheets. *Journal of Glaciology*, 2(18), pp.523-532.

Seguinot, J., Ivy-Ochs, S., Jouvet, G., Huss, M., Funk, M. and Preusser, F. (2018) Modelling last glacial cycle ice dynamics in the Alps. *The Cryosphere*, 12(10), pp.3265-3285.

Sternai, P., Herman, F., Valla, P.G. and Champagnac, J.D. (2013) Spatial and temporal variations of glacial erosion in the Rhne valley (Swiss Alps): Insights from numerical modeling. *Earth and Planetary Science Letters*, 12(10), 368, pp.119-131.

Sternai, P., Sue, C., Husson, L., Serpelloni, E., Becker, T.W., Willett, S.D., Faccenna, C., Di Giulio, A., Spada, G., Jolivet, L. and Valla, P. (2019) Present-day uplift of the European Alps: Evaluating mechanisms and models of their relative contributions. *Earth-Science Reviews*. https://doi.org/10.1016/j.earscirev.2019.01.005

Strandberg, G., Brandefelt, J., Kjellström, E. and Smith, B. (2011) High-resolution regional simulation of last glacial maximum climate in Europe. *Tellus A: Dynamic Meteorology and Oceanography*, 63(1), pp.107-125.

Višnjević, V., Herman, F. and Podladchikov, Y. (2018) Reconstructing spatially variable mass balances from past ice extents by inverse modeling. *Journal of Glaciology*, 64(248), pp.957-968.

Watts, A.B. (2001) Isostasy and Flexure of the Lithosphere. *Cambridge University Press*.

Wu, H., Guiot, J., Brewer, S. and Guo, Z. (2007) Climatic changes in Eurasia and Africa at the last glacial maximum and mid-Holocene: reconstruction from pollen data using inverse vegetation modelling. *Climate Dynamics*, 29(2-3), pp.211-229.